



Numerical investigation and experimental validation about negative overlap in Savonius hydrokinetic turbine

Ravi S. Patel¹ · Vimal K. Patel¹

Received: 8 February 2023 / Accepted: 2 November 2023 / Published online: 26 November 2023
© The Author(s), under exclusive licence to The Brazilian Society of Mechanical Sciences and Engineering 2023

Abstract

Conventional hydroelectric turbines use the potential energy of the water as a primary source of energy. However, the hydrokinetic turbines use the kinetic energy of the flowing water to generate power output. It is also one of the best clean energy generation technologies. Out of many hydrokinetic turbines, the Savonius hydrokinetic turbine is very simple in design and easy to manufacture. The ratio of the gap between the two vanes to the turbine diameter is known as the overlap ratio. The effect of the positive overlap has been extensively investigated for the Savonius turbine. However, for the first time in the present investigation, the effect of the negative overlap ratio on the hydrodynamic performance of the Savonius turbine is investigated. The highest value of negative overlap ratios is obtained for two, three, and four numbers of blades of Savonius hydrokinetic turbines. With the present investigation, the best-suited range of the negative overlap ratio is obtained for each case. The present investigation also concludes that the Savonius turbine with three and four vanes, with a negative overlap ratio, maintains its good performance for a wide variation in the turbine load. Also, the best-obtained design through numerical analysis was cross-verified by experiments.

Keywords Applied energy · Hydropower · Renewable energy · Savonius turbine · Negative overlap ratio · Hydraulic turbine

List of Symbols

| | | | |
|-------|--|-----------|---|
| OR | Overlap ratio $\left[\frac{e}{D}\right]$ | OR | Overlap ratio [e/D] |
| C_p | Coefficient of power $\left(\frac{2P_{out}}{\rho AV^3}\right)$ | P_{in} | Power available in flowing water $\left[\frac{1}{2}\rho AV^3\right]$ |
| C_t | Coefficient of torque $\left[\frac{C_p}{TSR}\right]$ | P_{out} | Power developed by turbine $[T \times \omega]$ |
| D | Diameter of rotor [m] | R | Radius of Rotor [m] |
| d | Diameter of vane [m] | r | Instantaneous torque radius or instantaneous distance from the resultant force to the center of the rotor [m] |
| e | Eccentric portion between vanes or gap between blades [m] | T | Torque available at the turbine rotor shaft [Nm] |
| F_d | Drag force (N) | τ_w | Wall shear stress [Pa] |
| F_l | Lift force (N) | u_f | Friction velocity |
| FSI | Fluid-structure interaction | V | Free stream velocity of flow [m/s] |
| H | Height of vanes [m] | Y | Normal distance from the wall |
| HKT | Hydrokinetic turbine | ρ | Density of fluid [kg/m ³] |
| k | Turbulent kinetic energy | ω | Specific dissipation rate |
| | | θ | Angle of rotation of vane [°] |
| | | SST | Shear stress transport |
| | | TSR | Tip speed ratio |
| | | CFD | Computational fluid dynamics |

Technical Editor: Daniel Onofre de Almeida Cruz.

✉ Vimal K. Patel
vimal.iitbombay@gmail.com

¹ Advanced Fluid Mechanics and Fluid Power Laboratory, Mechanical Engineering Department, Sardar Vallabhbhai National Institute of Technology, Ichchhanath, Dumas Road, Surat, Gujarat 395007, India

1 Introduction

The conventional power generation method is mainly based on a non-renewable source of energy, which is limited in the earth's crust. Also, these sources contain the most dangerous problem of pollution. To overcome the problem of non-renewable sources of energy, the use of renewable sources of energy is preferable nowadays. Renewable forms of energy are available on the earth's surface in the form of solar energy, wind energy, ocean wave energy, hydrokinetic energy, etc. [20, 24, 25]. Solar energy has the disadvantage of seasonal availability, and wind energy has a problem with regional availability. The conventional hydropower plant harms the environment because it uses a hydro turbine.

Similarly, to utilise ocean energy, setup, installation, and power output fluctuation are the major challenges. Comparatively, the utilisation of hydrokinetic energy is feasible near the riverbank or canal region, even at a remote location too [21, 24, 25]. The general installation of the Savonius rotor for the hydrokinetic application is shown in Fig. 1. Also, the availability of this energy source is relatively more predictable. To extract the energy from flowing water, different types of hydrokinetic turbines are used. In the present work, the utilisation of canal-based hydrokinetic energy was investigated using a Savonius hydrokinetic turbine.

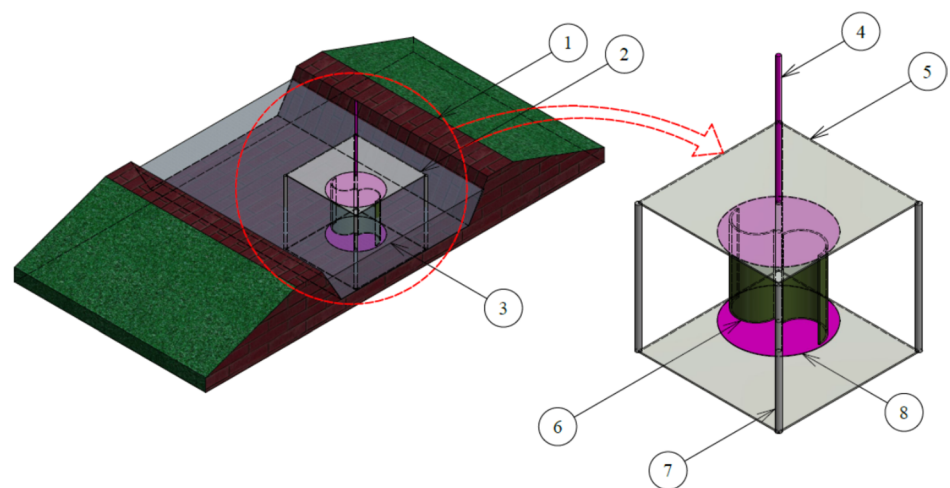
The use of the Savonius rotor was initiated for wind power extraction [28]. The Savonius turbine is explored experimentally by Santhakumar et al. [30] to generate energy from road highways. The Savonius wind rotor's

power output is much less than the same size as the Savonius hydrokinetic rotor. According to Betz, the maximum possible extraction from the flowing fluid is 59.3% of the supplied energy. The Savonius hydrokinetic turbine is predominantly a drag-force-driven turbine. It is simple in design, easy to manufacture, and has excellent starting characteristics [22]. The coefficient of power of the Savonius hydrokinetic turbine is comparatively less than that of the lift-force-driven Darrieus turbine of axial flow hydrokinetic turbines [3, 24–26]. Hence, there is a need to improve the performance of the Savonius hydrokinetic turbine. Many efforts are carried out to improve the Savonius turbine's performance by optimising the various design and operating parameters.

In order to estimate the power development by the Savonius rotor, a theoretical analysis was done by Patel et al. [24] using the impulse-momentum principle by pressure rise due to stagnation near the blades. The approach was compared with different values of the positive overlap ratio. A ready-to-use spreadsheet link is also given at the end of their article so that researchers can use it for further investigation. However, they have not investigated the negative values of Overlap.

The actual Savonius turbine's performance might not be the same as estimated using a laboratory-scale experimental setup performed in the laboratory canal if appropriate blockage correction is not considered during performance estimation. Patel et al. [21] suggested a straightforward and fundamental method for predicting an actual turbine's performance in a real canal. They suggested the velocity correction method to predict actual field turbine performance based on the laboratory experiments' results

Fig. 1 General setup layout



1. Canal, 2. Setup, 3. Water domain, 4. Extension shaft, 5. Frame plates,
6. Turbine Blades, 7. Framing rods, and 8. End plates

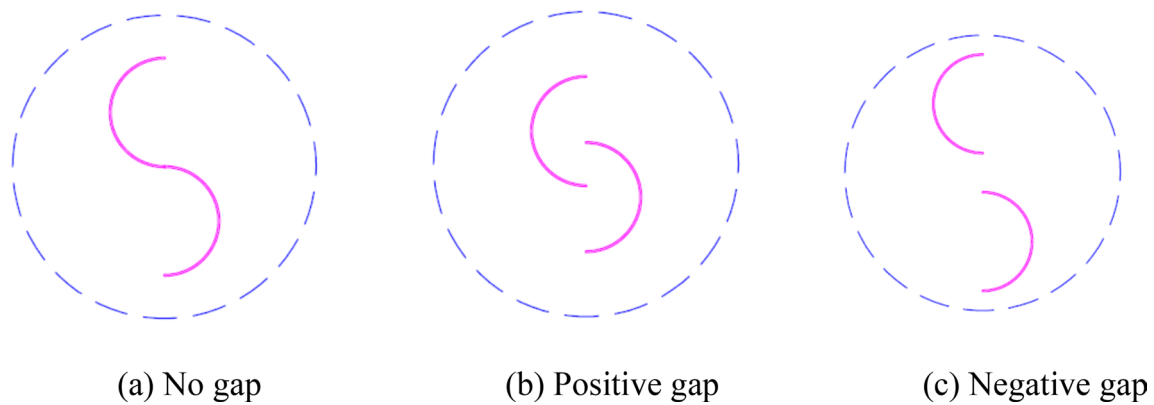


Fig. 2 Types of Overlap **a** Zero Overlap **b** Positive Overlap **c** Negative Overlap

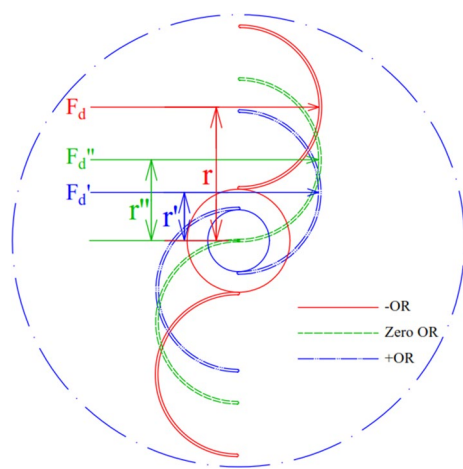


Fig. 3 Variation of torque with negative overlap

obtained from the laboratory-scaled turbine. The velocity correction methodology developed by them is specifically derived for hydrokinetic turbines to be operated in shallow water depths.

Patel et al. [22] investigated the effect of the endplate, Aspect ratio, and overlap ratio on Savonius hydrokinetic turbines. The results are explained with technical concepts and a complete fundamental discussion. They found that the presence of endplates enhances the rotor's performance; with an aspect ratio above 1.8, the C_p 's enhancement becomes stagnant, and with a positive overlap ratio of 0.11, the C_p value at its maximum.

The shape of the blade is a crucial parameter that determines the Savonius hydrokinetic turbine's performance. The 2D numerical simulations were done to find the drag coefficient for Benesh and modified Bach-shaped Savonius rotor by Alom et al. [2]. The experimental analysis was done for a two elliptical-bladed Savonius hydrokinetic

rotor by Talukdar et al. [34]; however, the performance of the conventional bladed rotor was observed superior.

In most of the analyses, two numbers of blades are investigated for the Savonius turbine. However, the experiment was carried out with two- and three-bladed Savonius hydrokinetic turbines by Talukdar et al. [34]. They concluded that the C_p value for a two-bladed rotor is higher than that of a three-bladed rotor. The numerical and experimental investigation was carried out for the three-bladed vertical axis Savonius rotor by Sarma et al. [31]. The effect of 6, 12, and 24 numbers of stator plates was analysed by Alexander et al. [1]. In the present investigation, the negative OR effect is investigated for two, three, and four blades. Fukutomi et al. show deflector superiority as a casing for cross-flow turbines [8]. A novel air-foiled-shaped deflector system was proposed to improve the performance of a Savonius wind turbine by Keyhan et al. [15]. They enhanced the static torque coefficient values up to two times higher than those generated by conventional Savonius turbines.

The investigation was also carried out for the multirotor turbine unit. Golecha et al. [10] analysed the performance of two turbines placed inline in the canal and found that with a gap ratio of eight, the upstream turbine's wake effect becomes negligible on the turbine placed on the downstream side. Rengma et al. [27] numerically and experimentally investigated the twin Savonius water turbines in a cluster. The minimum streamlines and spanwise distance required for even the Darrieus type of hydrokinetic turbine are investigated by Patel et al. [23]. The use of flexible blades [4], Nanoiber-based deflectors [7], porous deflector [33] are the immersing concepts used for the performance enhancement of Savonius turbine. Since major investigations were carried out based on the power coefficient, it is also considered a deciding parameter for investigation.

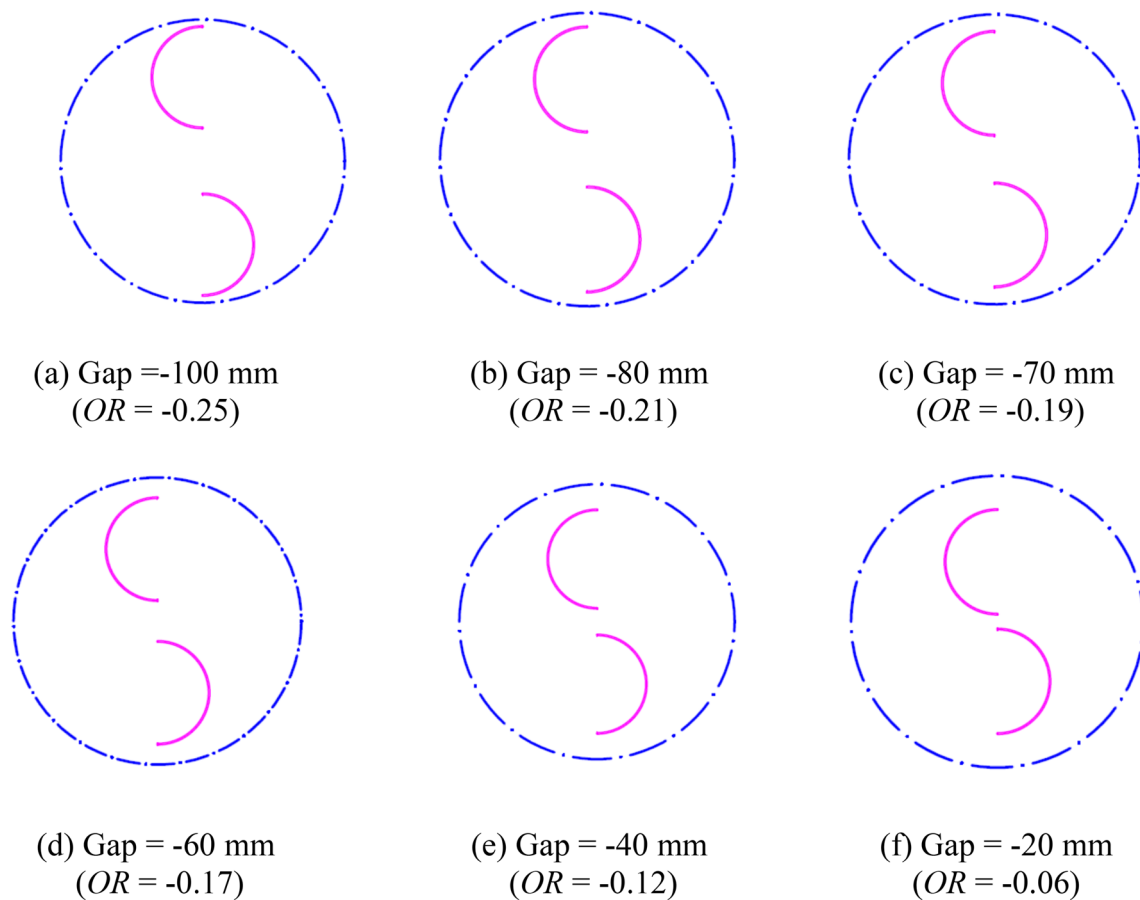


Fig. 4 Selected negative overlap ratios for the investigation

Table 1 Geometrical parameters

| Parameters | Values |
|-------------------|-------------------------------------|
| Diameter of Vanes | 0.15 m |
| No. of blades | 2 |
| Diameter of rotor | 0.3–0.4 m (dependent on Overlap) |
| Type of vanes | Semi-circular Straight bladed |

However, the torque generation depends on the magnitude of the net force on the vanes and the distance between the line of action of the net force and the centre of rotation (r). This distance (r) is termed an instantaneous torque radius in the manuscript. Mathematically, it is shown in Eq. (1). The power generation from the turbine can be enhanced if the torque development can be increased from the turbine rotor. The power output from the turbine can be correlated with the available torque on the shaft with Eq. (2).

$$T = r \times F_{net} \tag{1}$$

$$P = T \cdot \omega \tag{2}$$

2 Concept discussion

The Savonius rotor’s construction consists of two blades: One is the advancing blade, and the other is the retarding blade. The gap between the two blades is indicated by ‘e’. The flowing fluid strikes both the blades. The drag force on the advancing blade is higher compared to the retarding blade due to the concave shape of the second one.

One way to enhance the power output is to increase the torque on the vane. The torque on the vane can be increased by enhancing the net positive force’s magnitude on the vane and enhancing the instantaneous torque radius (r). The radius of the turbine increases when the overlap value is negative, and this is what mainly enhances the torque value, resulting in the turbine’s net performance in the present investigation. The importance of keeping the gap between the two vanes

Fig. 5 Domain size and boundary conditions

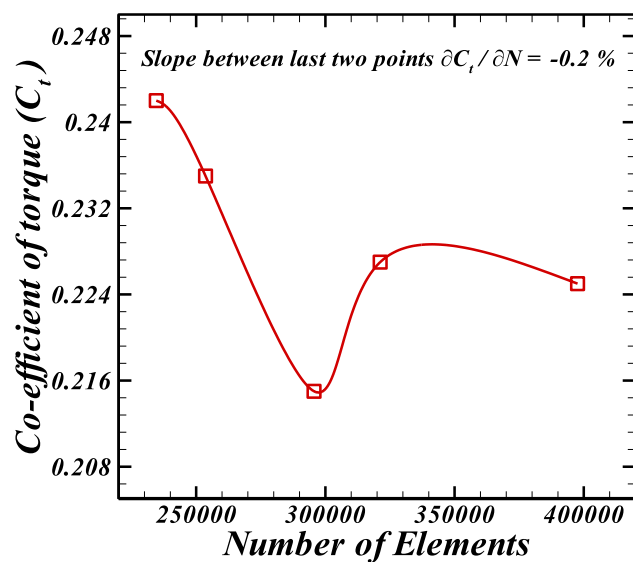
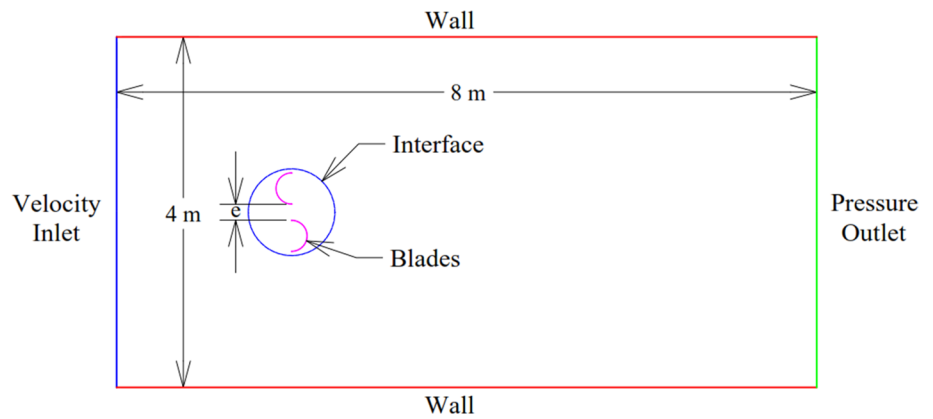


Fig. 6 Grid independent test

is explained conceptually and in detail by Patel et al. [22]. In their investigation, the gap was provided inside the two vanes in Fig. 2b. However, in the present investigation, the gap is kept outside of the turbine rotor’s vanes, as shown in Fig. 2c. So, two benefits can be achieved simultaneously; i. benefit of torque enhancement by increasing the torque radius (r) and ii. The benefit of torque enhancement by breaking the low-pressure region behind the retarding vane using the water bypass by providing a gap between them. Generally, the ratio of a positive gap to the rotor diameter is indicated as an overlap ratio. Hence, the provision of a negative gap is termed with a non-dimensional term as a negative overlap ratio in the present investigation.

Three different cases of the OR are shown in Fig. 3. i. Positive OR, ii. Zero OR and iii. Negative OR. In a positive OR case, the water from the advancing blade bypasses the vane’s gap and breaks the negative pressure region on the retarding vane’s downstream side. Hence, net positive torque is enhanced by reducing negative torque. However, in this case, the torque radius (r') is subsequently falling. Hence, the benefit of net force enhancement becomes limited. In the case of zero OR, the torque radius (r'') is increased compared to the positive OR case. Still, a strong negative force generation behind the retarding vane limits the net positive torque. However, in the case of negative OR, the benefit of enhanced torque radius (r) and breaking of the negative pressure region behind the retarding vane can be achieved. Hence, it is expected to get high performance from the negative OR with the Savonius turbine vanes.

3 Study of negative overlap ratio for two-bladed Savonius rotor

The optimum OR selection is critical because an excessively higher overlap ratio decreases performance even with a zero overlap ratio. Patel et al. [22] carried out an exhaustive study regarding the effect of overlap ratios and various aspect ratios, with a conceptual discussion behind the obtained results. Gupta et al. investigated the broader range of positive overlap ratios for the Savonius hydrokinetic turbine. Gupta et al. [11], Kamoji et al. [12], and Liang et al. [16]. They obtained an optimum overlap ratio of nearly 0.1 for a Savonius turbine with the hydrokinetic application. However, the effect of the negative overlap ratio on the Savonius turbine’s performance has not been investigated in depth in the current literature. Hence, in the present investigation, it

Table 2 Grid size for all selected overlap ratios

| Overlap ratio | 0 | 0.13 | 0.27 | 0.40 | 0.53 | 0.66 |
|---------------|---------|---------|---------|---------|---------|---------|
| Grid size | 342,562 | 346,449 | 344,256 | 345,908 | 347,529 | 346,875 |

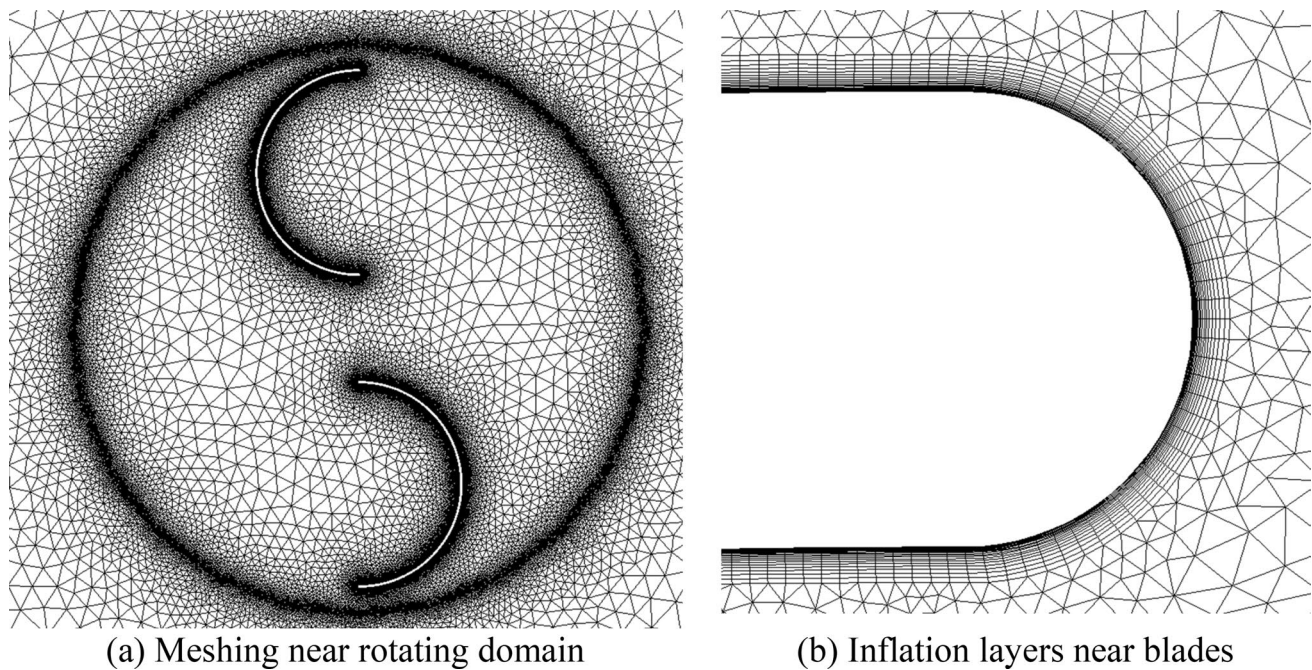


Fig. 7 Meshing used in the present investigation

is decided to investigate six different negative overlap ratios to investigate the performance of the Savonius turbine. The selected values of the overlap ratios, along with the sketch, are shown in Fig. 4. The vane diameter is kept the same, 150 mm in all the cases, and the gap between the vanes is varied, as shown in Fig. 4.

The overlap ratio is calculated using Eq. (3)

$$\text{OR} = \frac{e}{D} \quad (3)$$

where e Gap between the blades, D Diameter of the rotor

In the present investigation, ANSYS (Fluent) is used for the numerical. The simulation is carried out according to the following sequence.

- (1) Geometry and Domain selection
- (2) Mesh selection (Grid independent and Time independent)
- (3) Fluent Setup (Turbulence model selection)
- (4) CFD Post (Results)

3.1 Geometry and domain selection

The conventional Savonius rotor has semi-circular, straight blades. So, the cross-section of the rotor remains constant in the third direction. For the three-dimensional numerical analysis, the time required for the simulation is relatively high compared to the two-dimensional simulation. Hence, for the present study, a two-dimensional analysis

was performed for investigation. In the present study, six different values of negative overlap ratios are selected, as shown in Fig. 4. The obtained results are represented with non-dimensional terms like coefficient of torque (C_T), tip speed ratio (TSR), and coefficient of power (C_p). The geometric parameters considered for the present investigation are shown in Table 1.

The computational domain size is selected considering the investigation done by Saini et al. [29] which has domain size of 1.7, 3.5 and 1.3D for front, back, and top–bottom, respectively and Daskiran et al. [5] which have 12.38 and 15.14D domain size. The results obtained from the analysis are independent of the domain size. The blockage value varies from 7.5 to 10% for the domain's selected size, which is even less than the domain size selected by Saini et al. [29]. The schematic of the domain and the selected boundary

Table 3 Time step size for each TSR and OR (Overlap ratio)

| TSR | 0.4 | 0.6 | 0.8 | 1.0 | 1.2 |
|-------|---------|---------|---------|---------|---------|
| OR | | | | | |
| 0 | 0.03927 | 0.02618 | 0.01963 | 0.01571 | 0.01309 |
| −0.06 | 0.04189 | 0.02792 | 0.02094 | 0.01675 | 0.01396 |
| −0.12 | 0.04451 | 0.02967 | 0.02225 | 0.01780 | 0.01483 |
| −0.17 | 0.04712 | 0.03141 | 0.02356 | 0.01884 | 0.01570 |
| −0.19 | 0.03209 | 0.02139 | 0.01604 | 0.01283 | 0.01069 |
| −0.21 | 0.04974 | 0.03316 | 0.02487 | 0.01989 | 0.01658 |
| −0.25 | 0.05235 | 0.03490 | 0.02618 | 0.02094 | 0.01745 |

Table 4 Reference values

| Parameters | Values |
|---------------------------|-----------------------------|
| Area | 0.30 to 0.40 m ² |
| Density | 998.2 kg/m ³ |
| Depth | 1 m |
| Length | 0.15 to 0.20 m |
| Pressure (Gauge Pressure) | 0 Pa |
| Velocity | 0.5 m/s |
| Reference zone | Rotor |

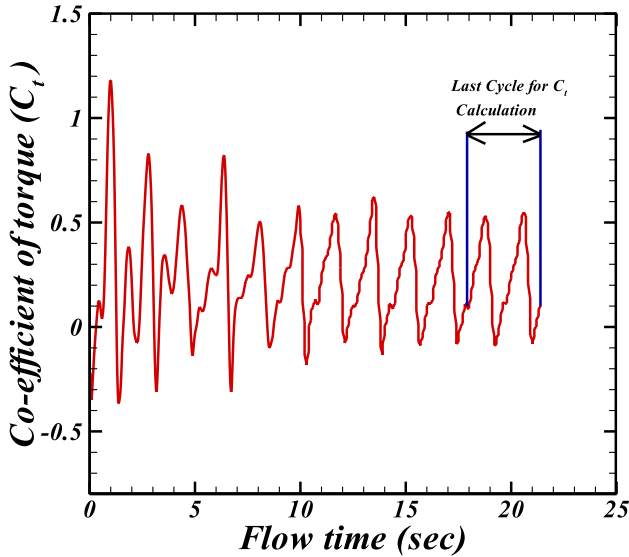


Fig. 8 Variation of Coefficient of torque with time

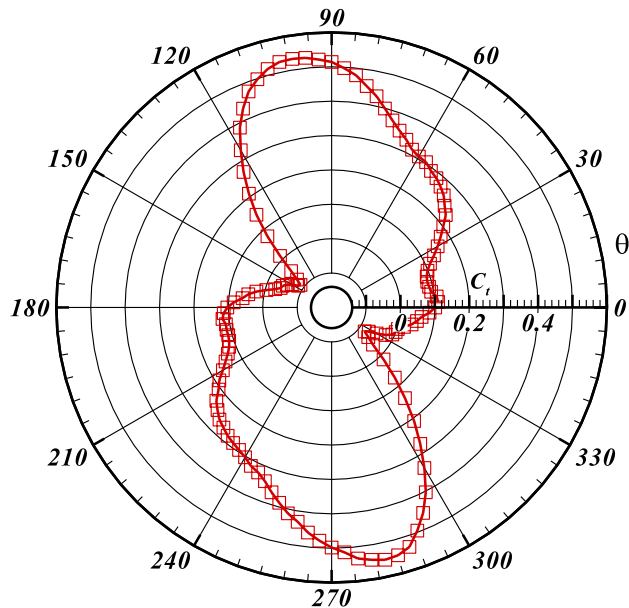


Fig. 9 Variation of coefficient of torque with the rotational angle

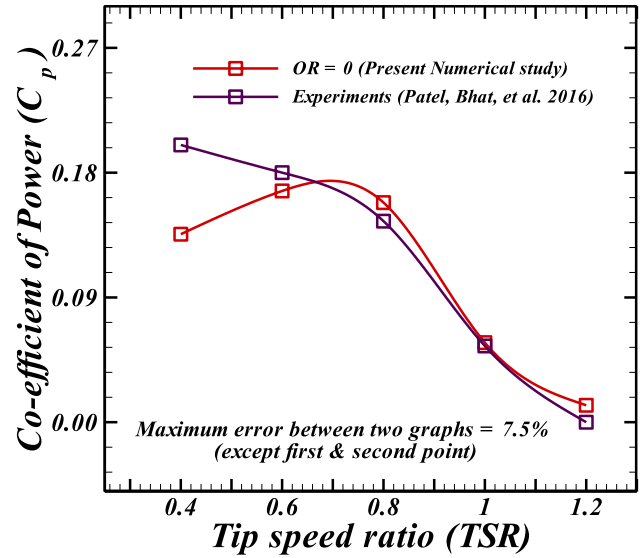


Fig. 10 Validation of Present work

conditions for the numerical analysis are shown in Fig. 5. To have a continuous flow from the stationary domain to the rotating domain, the same coinciding nodes are selected for the rotating domain’s outer surface and the inner surface of the stationary domain. The boundary condition considered for the present numerical investigations is shown in Fig. 5.

3.2 Mesh selection

The complete two-dimensional model of the rotating domain with a stationary domain was imported in the ‘MESH module’ of ANSYS. The unstructured mesh is generated in the mesh module of ANSYS, and an automatic mesh generation is used.

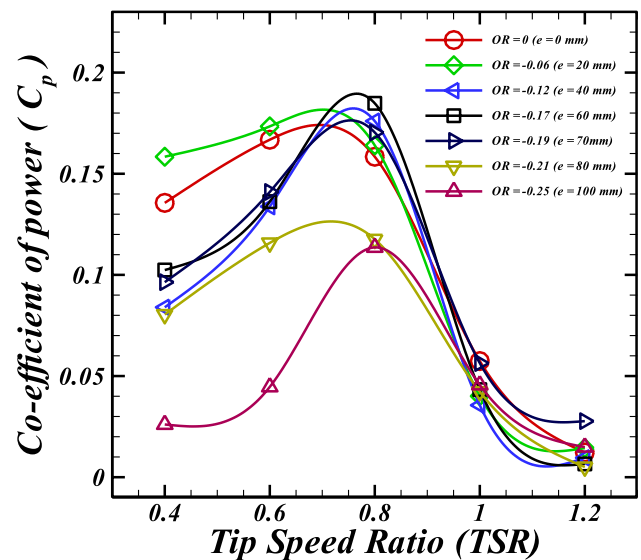


Fig. 11 Coefficient of power for different values of Overlap ratio

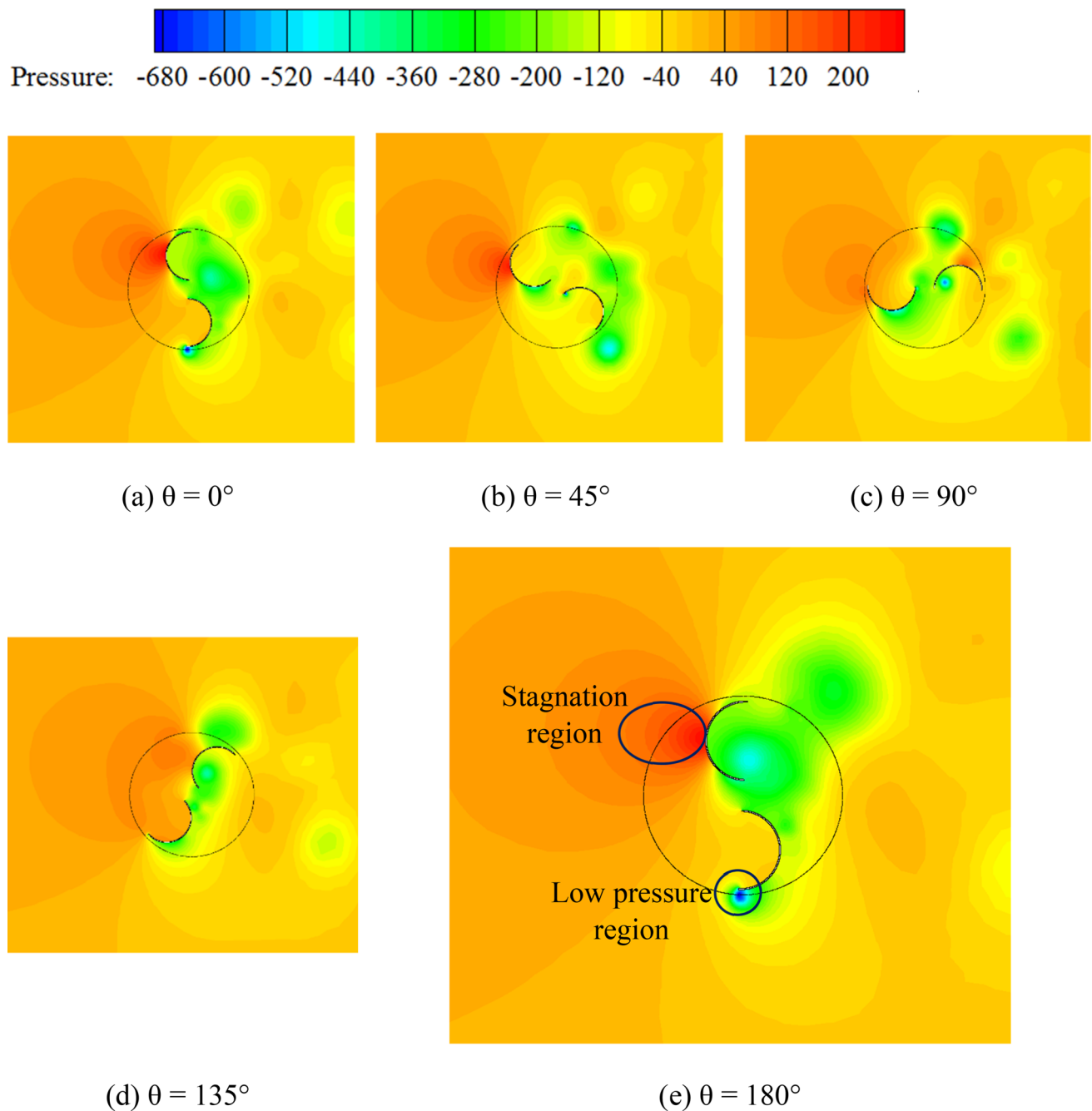


Fig. 12 Pressure Contours for different positions of blades

The results obtained from the numerical simulation are also affected by the mesh size and quality [9, 18]. In this regard, a grid-independent study is also carried out to determine the optimum mesh size. The coefficient of torque is calculated using different grid sizes for zero Overlap, keeping other parameters the same. The obtained values of C_t are presented for different grid sizes, i.e., the number of elements, which is shown in Fig. 6. From the result, it can be observed that the variation in the obtained values of C_t becomes negligible after

the number of volumes used exceeds 320,000. The slope of the graph between the last two points becomes -0.2% . Hence, the results obtained after 320,000 volumes can be considered grid-independent results. The selected numbers of the elements for investigation-specific overlap ratios are shown in Table 2.

As the variation of the velocity gradient near the wall is stiffer, the mesh density near the wall must be high. The inflation layers applied at the walls improve the mesh's quality and provide better boundary layer separation near the wall.

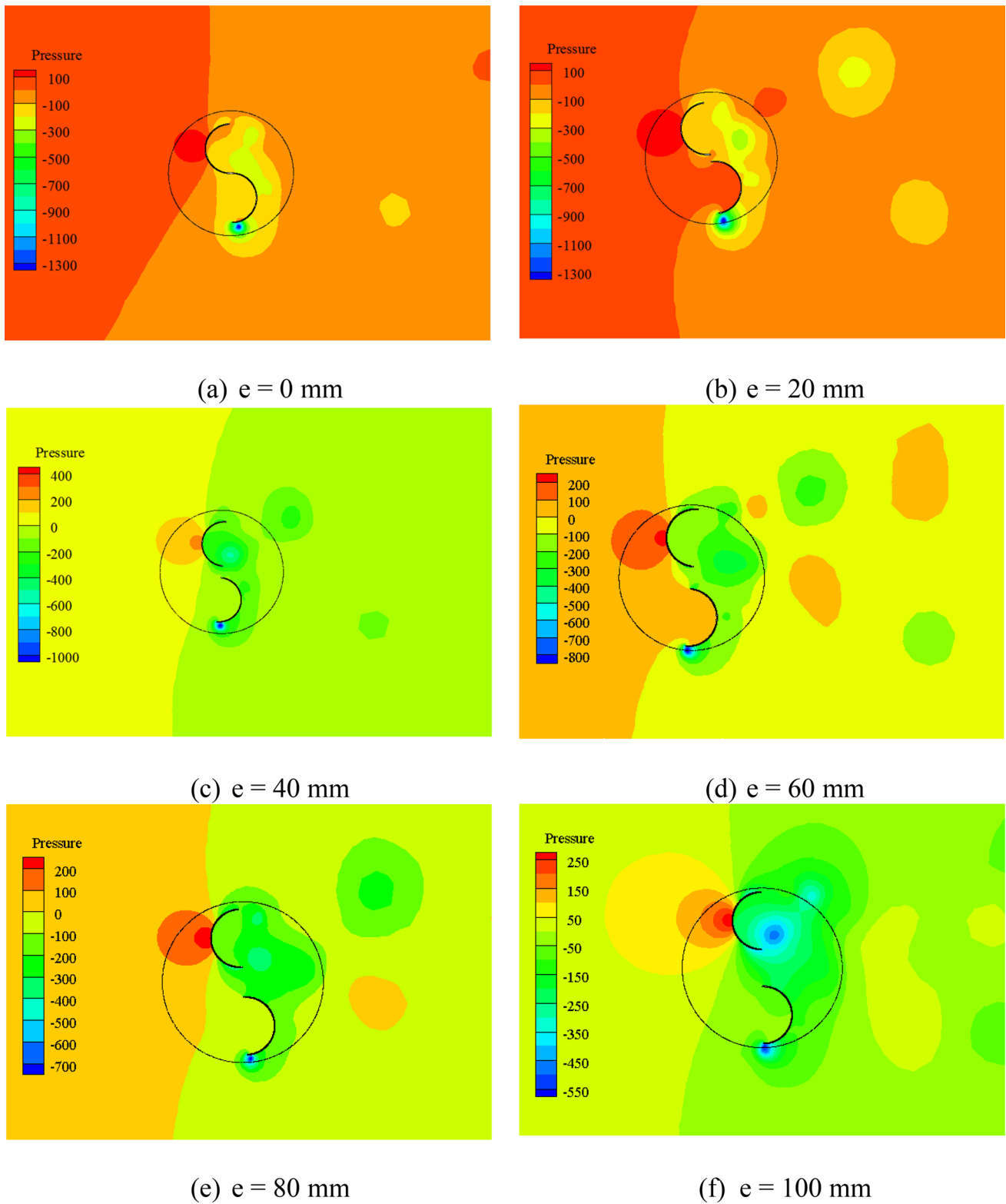


Fig. 13 Pressure Contours for different gaps between blades

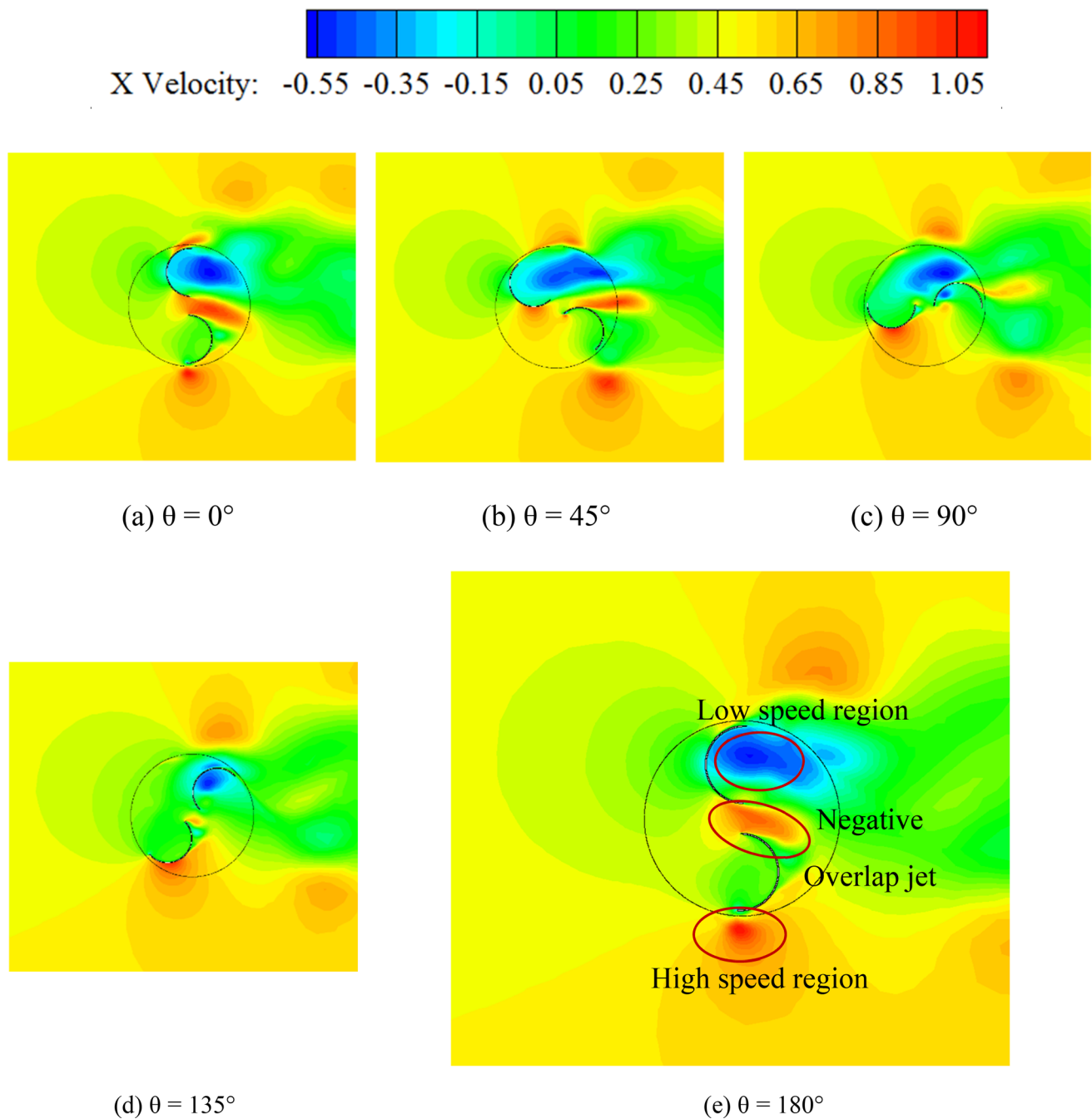


Fig. 14 Velocity Contours for different positions of blades

The mesh's quality near the wall surface is governed by wall y^+ (dimensionless wall distance from the centroid of the first cell above the wall). The value of y^+ depends on the height of the first cell near the wall. The appropriate value of y^+ predicts the velocity profile near the real pattern. Thus, the value of y^+ should be less than one [13, 17, 19, 29]. For the present case, the obtained minimum and maximum y^+ values are 0.00103 and 0.13479, respectively.

$$y^+ = \frac{\rho u_f y}{\mu} \tag{4}$$

where, $u_f = \frac{\tau_w}{\rho}$

$$\tau_w = \left(\frac{\mu du}{dy} \right)_{y=0}$$

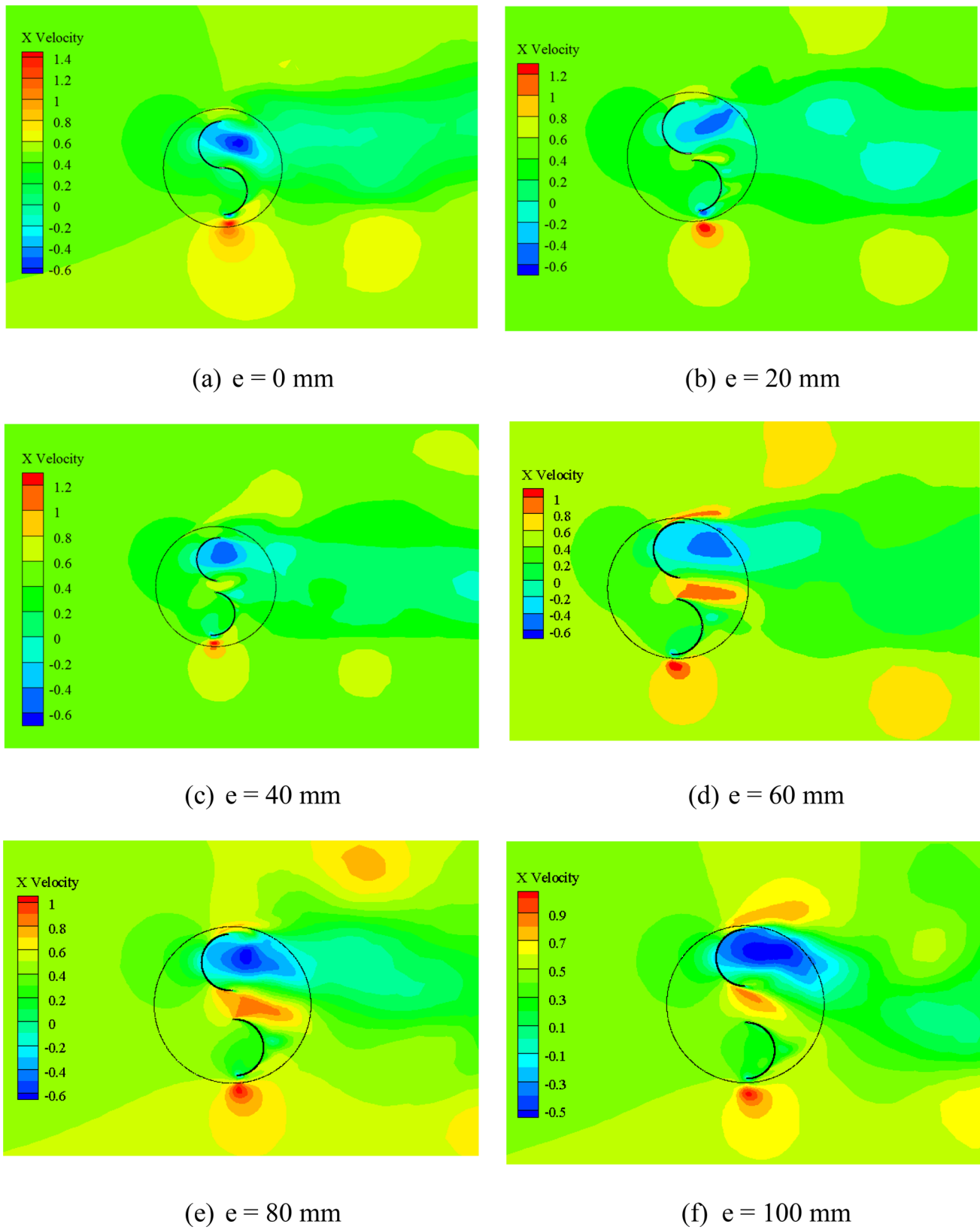


Fig. 15 Velocity Contours for different gaps between blades

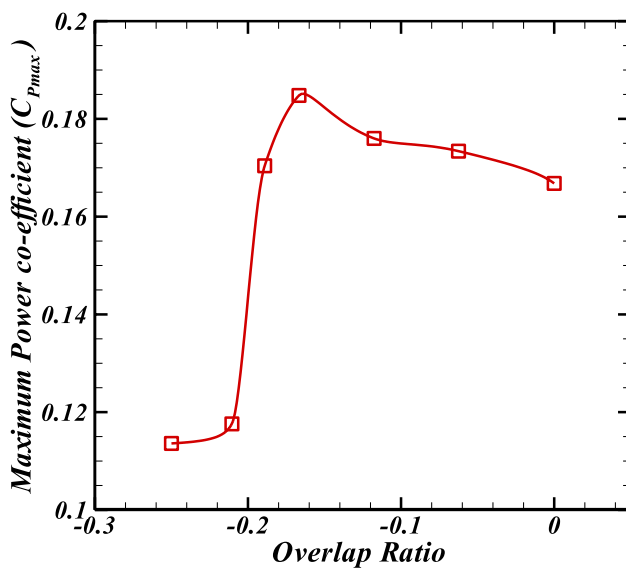


Fig. 16 Coefficient of power variation with Negative Overlap Ratio

For the selected grid size, the average values of orthogonal quality, maximum skewness, and maximum aspect ratio were observed as 0.98, 0.81, and 68.15, respectively. These values indicate the outstanding quality of the mesh [14]. After all considerations, triangular elements were selected with 20 inflation layers with a growth rate of 1.15. The obtained mesh is shown in Fig. 7.

3.3 Fluent setup

After meshing, the stationary domain and the rotating domain are imported to the setup module of ANSYS Fluent. The two-dimensional, unsteady, incompressible Navier–Stokes equations were discretised using the finite volume method. A

second-order upwind scheme was used to solve the unsteady part of the URANS equations. Suitable boundary conditions were applied to the setup for unsteady Reynolds-Averaged Navier–Stokes (URANS) equations to observe the flow pattern. Boundary conditions used in numerical simulations are shown in Fig. 5. As suggested by Fertahi et al. [6] the inlet condition was selected as a velocity inlet (Dirichlet), as fluid enters with a fixed value of velocity, and the outlet condition was a pressure outlet (Dirichlet) [6]. The top and bottom edges of the flow domain were kept as “wall” boundary conditions [32]. To estimate the selected hydrokinetic turbine’s performance, the water liquid was used as the working fluid by keeping water properties as default in the software. Further, the turbine blades were assigned as wall conditions (no-slip wall) to both blades. For the interaction between the rotor and stationary domain, an interface boundary condition is assigned at the outer surface of the rotating domain (int1) and the inner surface of the stationary flow domain (int2).

3.3.1 Turbulence modelling

The flow visualisation can be carried out using a turbulence model. The commercial code solves these equations for all discretised finite volumes. The $k-\omega$ SST turbulence model is the two-equation updated form of the baseline (BSL) model, which smoothly bridges the $k-\omega$ and $k-\epsilon$ models. This model facilitates visual flow behaviour near the wall using the $k-\omega$ definition, where the boundary layer predominates. The $k-\epsilon$ description helps visualise flow behaviour away from the wall, where the boundary layer effect is negligible and the transformation from near the wall to away from the wall.

To determine precise results concerning time, a sufficiently small time step would be selected. For each tip speed ratio, a time step was defined for 3° rotation of the turbine. In the present study, the diameters of seven selected geometries

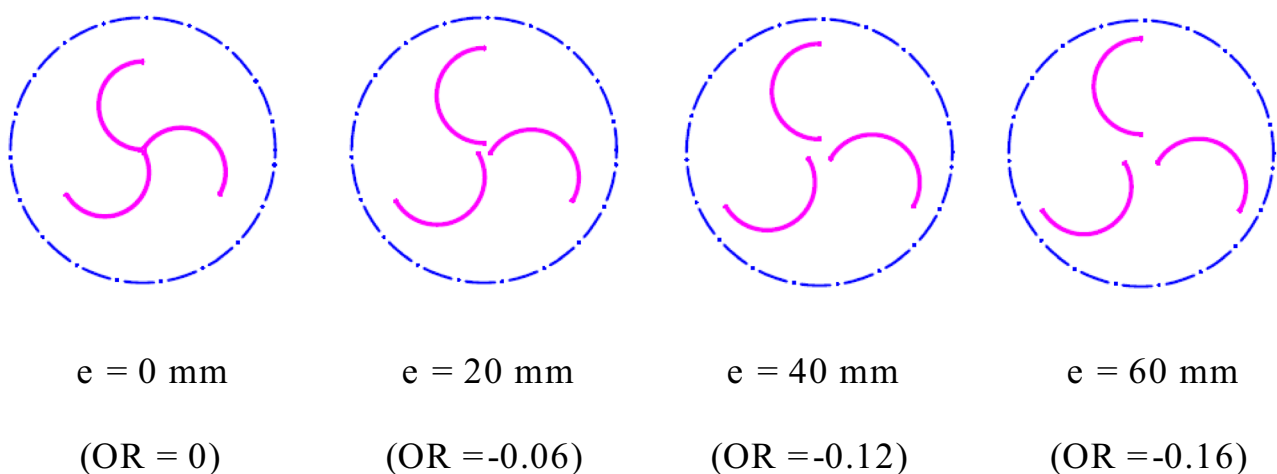


Fig. 17 Negative Overlaps with three vanes for Savonius rotors

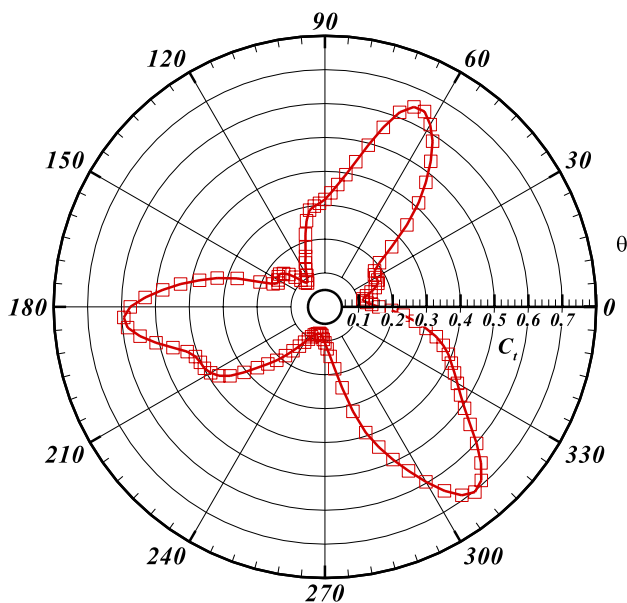


Fig. 18 Coefficient of torque for three-bladed rotor

are different; hence, the time step size for all geometries is different and is presented in Table 3. Moreover, the simulation was run for six complete rotations, with each revolution completed in 120-time steps, and 200 iterations were given for each time step to ensure a time-independent result. The SIMPLE scheme estimated the pressure–velocity coupling, and the equations for pressure, momentum, and turbulence were discretised with a second-order system. The detailed system used for simulation has seven numbers of logical processor (Processor: i7, 3.5 GHz) with 8 GB RAM. The approximate time taken for one simulation of five revolutions is 11 h.

The results obtained by the numerical simulation are discussed in the result and discussion section.

3.4 Results and discussion

The obtained results are presented in the form of the non-dimensional terms, coefficient of power (C_p), coefficient of torque (C_t), and TSR. For the valid output from the numerical simulation, the setup of reference values is essential. The considered reference values for the present investigation are shown in Table 4.

The obtained graph of the coefficient of torque with flow time for 0.8 TSR is shown in Fig. 8. The diagram is shown for the -0.17 overlap ratio. The chart indicates that the value of C_t is not constant for different angular positions of blades. For the first 10 s of flow time, the fluctuation of C_t is very random, but after 10 s, the fluctuation pattern becomes constant, which confirms the steady-state result.

Figure 9 indicates the variation of coefficient of torque (C_t) after reaching the steady-state condition. It is taken from the last calculated cycle from Fig. 8. For determining the coefficient of power, the average value of C_t was taken from Fig. 8. The obtained C_p for different five TSR values is shown in Figs. 10 and 11. The obtained results are compared with the results obtained by Patel et al. [22] derived from the experimental study. The comparison of the results is indicated in Fig. 10.

The close matching of the obtained results validates the methodology used in the present investigation. The small variation in the results might arise due to different overlap ratios of the considered rotor and the uncertainty associated with the experimental results. However, the variation of the co-efficiency of power with the tip speed ratio is quite similar, confirming the present methodology's validity. The value of C_p increases with TSR up to 0.8, then drastically decreases from 0.8 to 1.2 TSR. The maximum value of the C_p is observed between 0.6 and 0.8 TSR for all selected overlap ratios.

3.4.1 Pressure contours

To understand the flow behaviour near the turbine region and behind the turbine vane, pressure and velocity contours are presented and discussed. Figure 11 is plotted for the wide range of the overlap ratio, including an extensive range of tip speed ratios; however, the contours are presented for a TSR value of 0.8 only where the power coefficient was found to be highest. The entire numerical study was done for Reynolds number ranging from 1.49×10^5 to 1.99×10^5 .

Figure 12 shows the different azimuth orientations of the rotor vanes. The detailed observation is shown in Fig. 12e. The red-coloured region in all figures shows a high-pressure region as the fluid particles stagnate at these locations. The reason can be justified as the intensity of the pressure is even higher at the retarding vane due to the vane's velocity obstructing the fluid flow in the opposite direction. Similarly, the low-pressure region forms on the downstream side of the retarding vane. Also, to maintain the flow, a low-pressure region forms near the outer end of the blades Fig. 13.

3.4.2 Velocity contours

The velocity contours are plotted at different vane azimuthal orientations, as shown in Fig. 14. The detailed observation is shown in Fig. 14e. The red-coloured region in all figures indicates the high-speed regions. The high-speed region is also observed between the two blades due to negative overlaps at the vanes' vertical orientation. This is due to the converging section formation between the vanes. Also, the vortices were formed behind the retarding blade due to the sudden expansion of the water jet. The high-velocity region is also observed

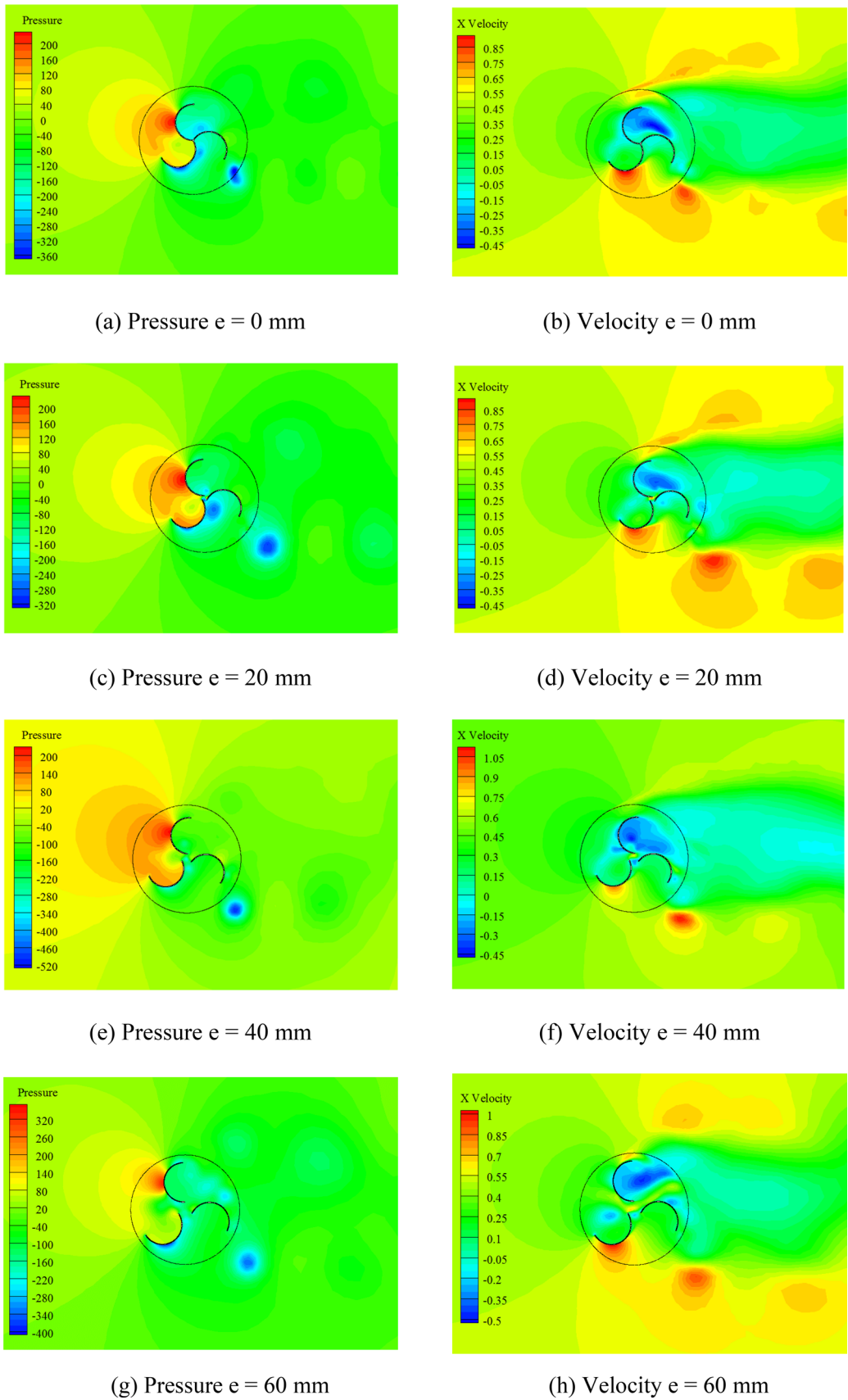


Fig. 19 Pressure and Velocity contours for three-bladed rotor

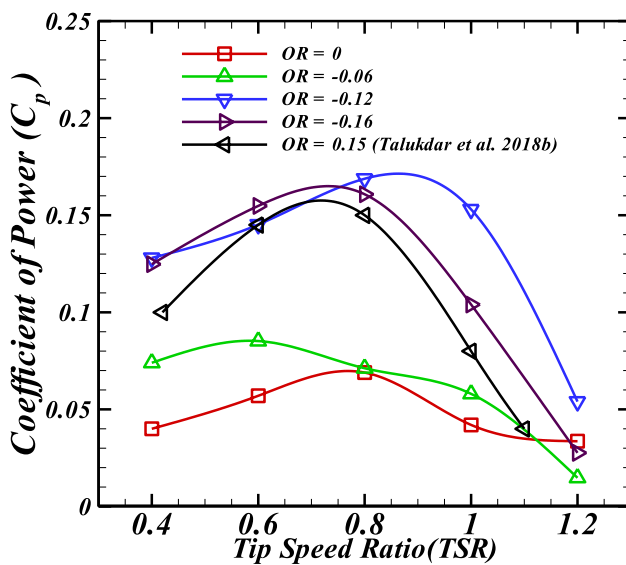


Fig. 20 Variation of Coefficient of Power with TSR

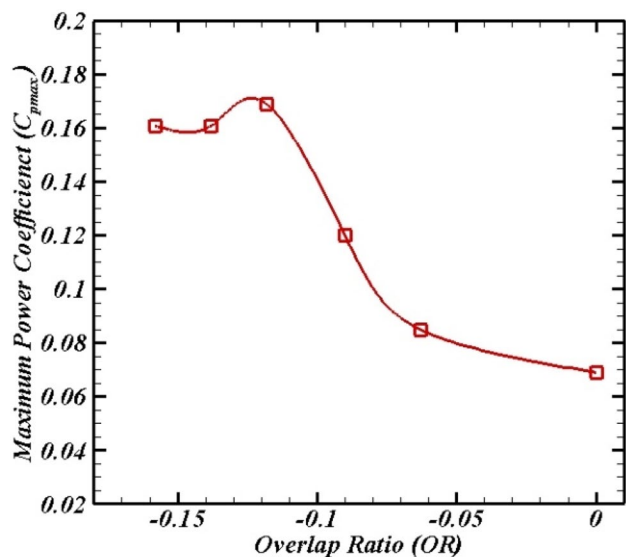


Fig. 21 Variation of Coefficient of power with negative OR

above and below the rotor zone. This is due to the diversion of the water stream due to the rotating vanes' resistance.

Figure 15 indicates the velocity contours at the vanes' vertical orientation for different negative overlaps between the vanes. It can be observed that for the gaps between the vanes of 0, -20, and -40 mm, the water velocity in between the vanes is relatively lower compared to the gaps of -60 and -80 mm. It indicates that the kinetic energy of water striking the vanes converts to pressure energy and subsequently produces the vanes' drag forces. However, the high-velocity region between

the vanes for the vane gap of -60 and -80 mm indicates that the stagnation pressure generated at the vane's upstream side is partially converted to gain kinetic energy. Hence, the fraction of energy conversion to the mechanical energy of the rotor can be reduced. Hence, when the gap between the vanes is too low, the energy conversion might be adversely affected due to excessive bypass of the water from the rotor region. On the other hand, the excessive gap between the vanes also adversely affects the energy convection from water flow by decreasing the stagnation pressure at the vane's upstream side, which may arise due to an excessive gap between the vanes.

To conclude the investigated negative overlap ratio, the maximum coefficient of power obtained from the entire range of TSR of the different overlap ratio cases is selected. The selected maximum coefficient of power is plotted against appropriate cases of overlap ratios, as shown in Fig. 16. The graph indicates the highest power coefficient, approximately 0.19, with an overlap ratio of -0.17 (a gap between the vanes of -60 mm). Figure 16 shows that, initially, by increasing the gap between the vanes (moving right to left), the performance enhancement is observed until the overlap ratio of -0.17 (gap -60 mm). This might be due to the efficient breaking of the negative pressure by the bypass water flow from the gap and the torque enhancement due to shifting the torque radius outward from the rotor's centre. However, by the gap enhancement beyond the overlap ratio of -0.17, a sudden drop in power coefficient is observed. This may be due to excessive water bypassing of the gap between the vanes.

4 Study of negative overlap ratio for three-bladed Savonius rotor

To investigate the vane's number, considering the negative overlap ratio, the investigation is extended for three and four vanes of the Savonius turbine. The investigation is carried out for three and four numbers of the vanes, considering four values of the vanes' gap. The schematic diagram of the negative overlap considered for the investigation of three blades is shown in Fig. 17.

Considering the same domain size, the rotating domain was replaced by the three-bladed rotor. Again, simulations are carried out, keeping all boundary conditions similar to the validated two-bladed rotor analysis. The obtained coefficient of moment for a three-bladed Savonius rotor is shown in Fig. 18. The obtained pressure and velocity contours are shown in Fig. 19, at the 90° orientation. The contours indicated a similar pattern as in two-blade analysis, i.e., for pressure contours, the front side of the blade experienced high pressure. But due to the blade being oriented at 120° from the vertical blade, some flow streams

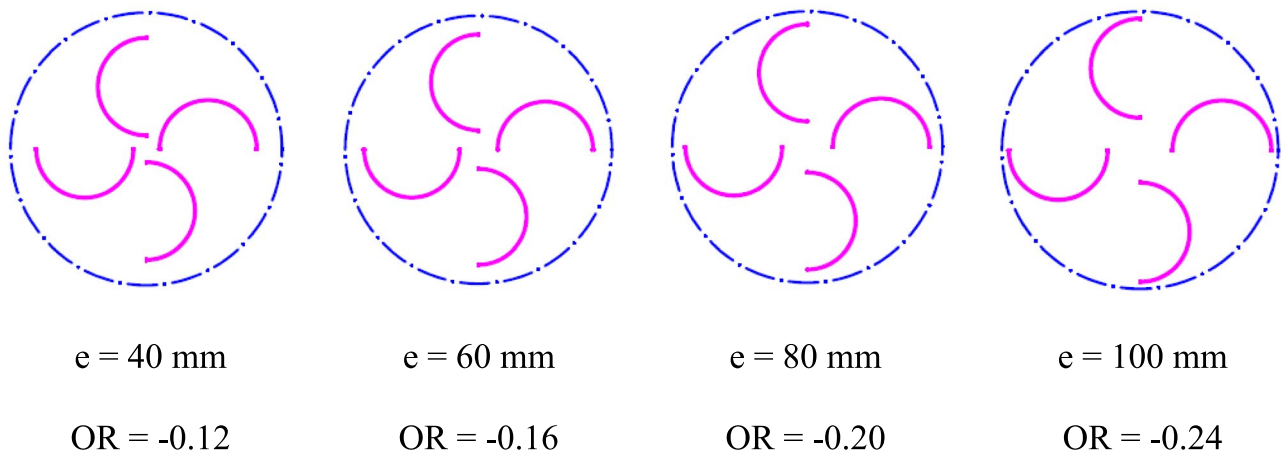


Fig. 22 Negative overlap values for four-bladed Savonius rotor

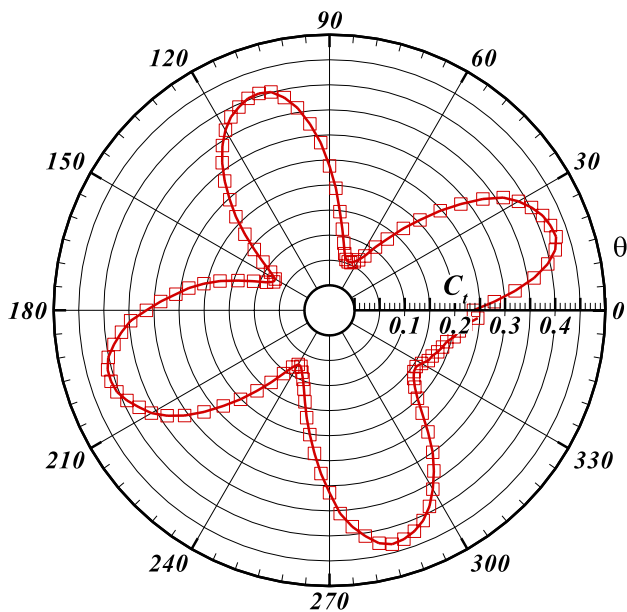


Fig. 23 Coefficient of moment for four-bladed rotor

are getting diverted towards the retarding blade, which causes the negative torque observed in Fig. 19.

In contrast, the backside of the blade indicates a low-pressure region. From the velocity contours, it is observed that the high-speed regions are observed nearly around the edge of the front side blades, where boundary layer separation takes place. Further, at the turbine rotor's downstream side, vortices were observed due to periodic boundary layer separation due to the blades' rotations.

To get the best negative overlap ratio, the variation of the maximum coefficient of power obtained with different values of negative overlap is shown in Fig. 20. The results

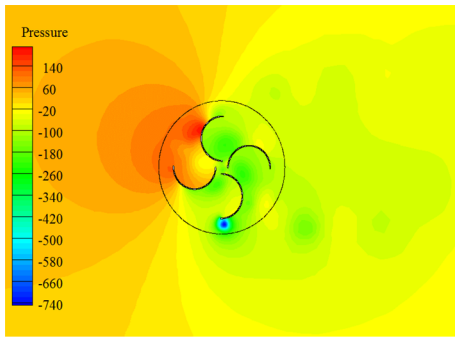
indicate a maximum co-efficiency of power of 0.169 with a negative overlap ratio of -0.12 , which is more than the positive overlap ratio investigated by Talukdar et al. [34]. Results indicate the maximum coefficient of power between -0.12 and -0.15 for the three-bladed Savonius rotor Fig. 21.

5 Study of negative overlap ratio for four-bladed Savonius rotor

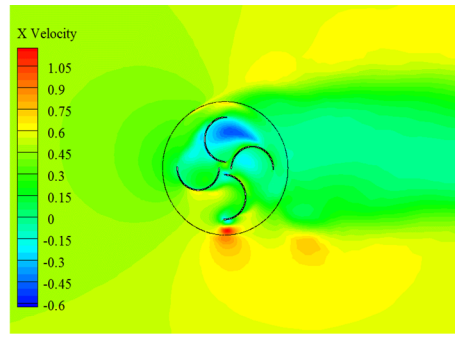
A similar study was also carried out for a four-bladed Savonius rotor. The selected overlap values investigated in the present investigation are shown in Fig. 22. The moment coefficient is plotted for the investigated values of negative overlap ratios, and the polar graph is shown in Fig. 23. The graph shows four peaks as a four-bladed graph.

Figure 24 indicates pressure and velocity contours for a four-bladed rotor. It is observed that the pressure on the advancing blade decreases compared to two-bladed and three-bladed rotors. The decrease in pressure over the advancing blade is due to the additional blade compared to two- and three-bladed turbines. Due to the same reason, the stream is getting diverted towards the retarding blade, which causes the development of negative torque, which is observed in Fig. 24.

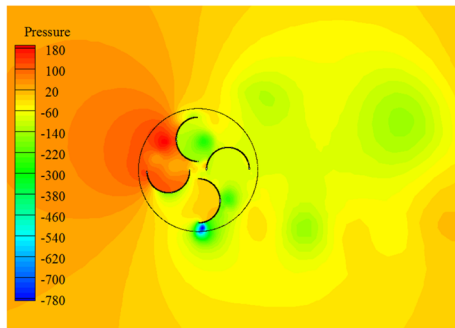
This is due to the additional blade placed between the advancing and retarding blades, which may restrict the mass flow rate of water striking the advancing vane and decrease the stagnation pressure rise. Hence, the co-efficiency of power's peak value is also lower compared to two-bladed and three-bladed rotors. Figure 25 indicates the variation of the power coefficient for different tip speed ratios for different negative overlaps of a four-bladed design. The maximum value of the power coefficient for different overlap ratios is plotted to get the negative overlap's best value for the four



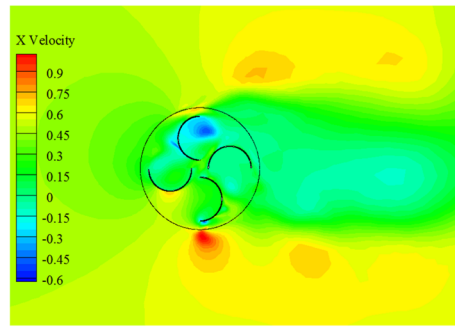
(a) Pressure contour $e = 40$ mm



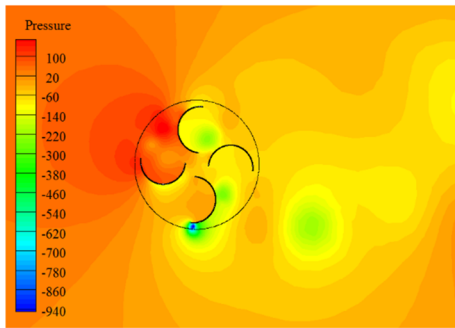
(b) Velocity contour $e = 40$ mm



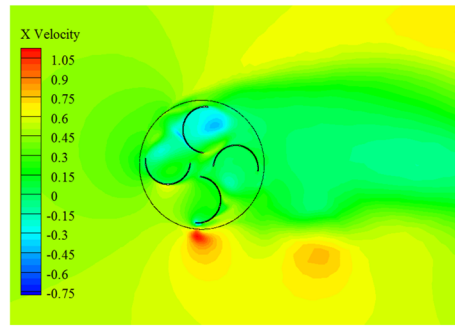
(c) Pressure contour $e = 60$ mm



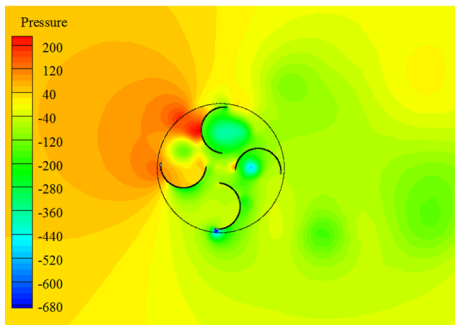
(d) Velocity contour $e = 60$ mm



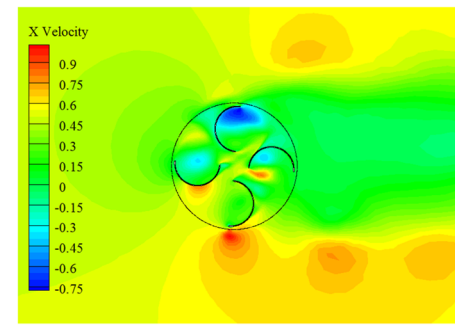
(e) Pressure contour $e = 80$ mm



(f) Velocity contour $e = 80$ mm



(g) Pressure contour $e = 100$ mm



(h) Velocity contour $e = 100$ mm

Fig. 24 Contours for all selected negative overlap

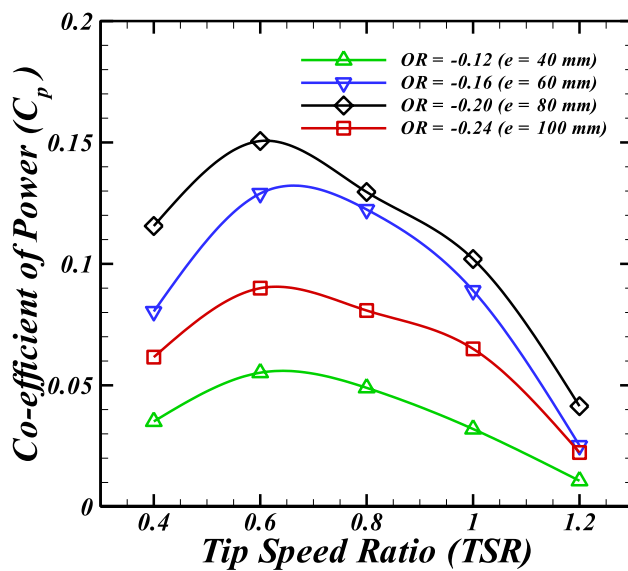


Fig. 25 Variation of Coefficient of power with TSR

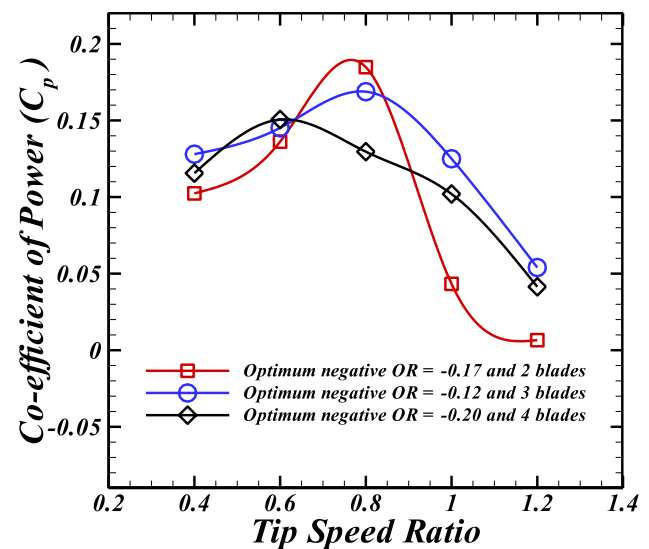


Fig. 27 Comparison between two-, three-, and four-bladed rotor for investigated OR

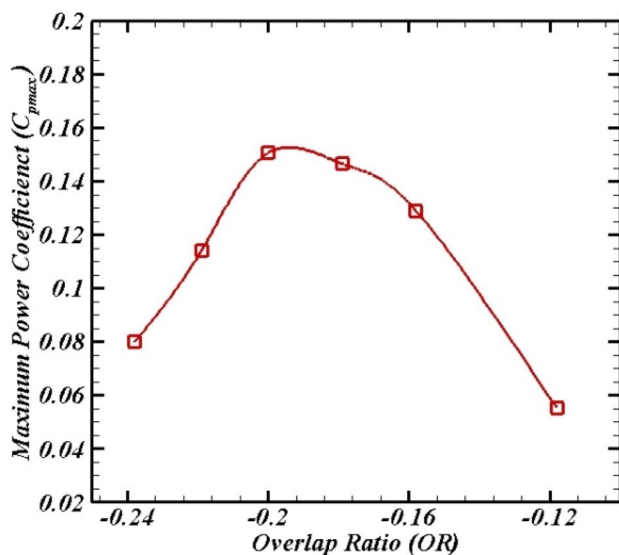


Fig. 26 Variation of Coefficient of power with negative OR

turbine vane design, as shown in Fig. 26. The results indicate the best value of the negative overlap ratio between -0.16 and -0.20 in the case of four vane turbine rotors.

To conclude the investigation, the best-performing results of negative Overlaps from all three cases, i.e., two vanes, three vanes, and four vanes of the turbine, are simultaneously marked on one chart for better comparison. The comparison of the results obtained from the present investigations is shown in Fig. 27.

The result indicates the highest value of the efficiency of power 0.18 at a tip speed ratio of nearly 0.8 with a

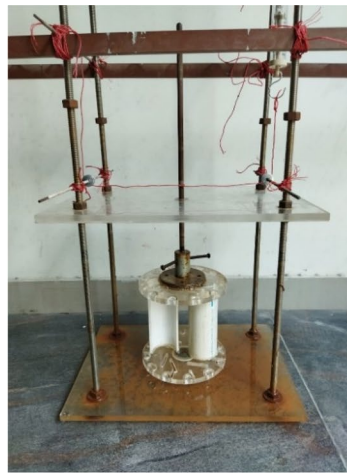
two-bladed turbine rotor. Still, the rate of rise and fall of performance is also very steep for two-bladed turbine rotors, near the power region's maximum coefficient. Hence, in the case of a minor change in the load on the turbine rotor (with a minor change in the tip speed ratio) from the maximum C_p location, the performance deteriorates very drastically. Hence, two-bladed turbine rotors are suitable only for those sites where the load on the turbine remains nearly constant, keeping the operating speed nearly TSR of 0.8 at the highest C_p .

On the other hand, the maximum power coefficient obtained with three-bladed turbines is less than that obtained with the two vane turbines. However, it provides nearly consistently good performance for a wide range of loads, i.e., tip speed ratio. A similar trend is also observed for the four-bladed turbine rotor. Hence, a three-bladed turbine rotor is a comparatively better option where load fluctuation on the turbine is relatively high, despite its maximum coefficient of power being less compared to the two-vaned turbine rotor.

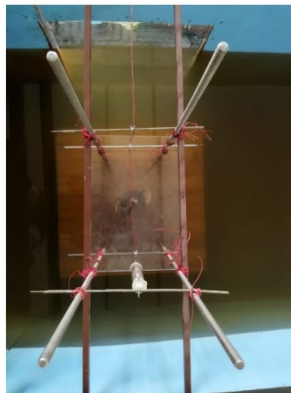
The numerical analysis's primary purpose is to find the best performing design, and after obtaining it, the best-obtained design should be tested experimentally.

6 Concluding experiments

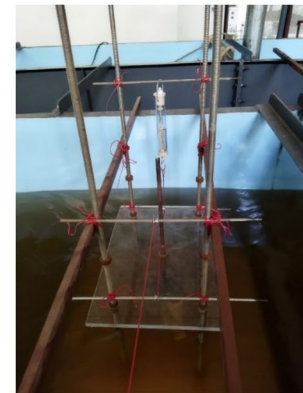
The two-bladed Savonius hydrokinetic turbine performs better on the power coefficient performance parameter; hence, the two-bladed Savonius rotor was fabricated and examined. The details of the experiments are mentioned in the following subsections:

Fig. 28 Experimental setup with installation in channel

(a) Experimental setup



(b) Top view of setup inside channel



(c) Side view of setup inside channel

Table 5 Dimensions of rotor

| Reference dimensions | Values |
|----------------------|---------|
| Number of blades | 2 |
| Diameter of rotor | 0.12 m |
| Diameter of blades | 0.05 m |
| Gap between blades | 0.02 m |
| Thickness of blades | 0.005 m |

6.1 Experimental setup

The experiments were performed using the best configurations obtained from CFD analysis. The setup was prepared with four studs used as supporting frames. Two transparent acrylic sheets were provided to support the rotor's ends. The two metallic flanges were machined and attached to the endplates of the rotor. The top flange provided a hole for the turbine shaft. The PVC pipe was cut such that it generated two C-shaped Savonius blades, as shown in Fig. 28a. The selected dimensions of a rotor are mentioned in Table 5.

The prepared setup was then installed in an available artificial canal using two supporting rectangular cross-sectioned rods, as shown in Fig. 28b and c. Also, the experimental setup was mounted with a spring balance arrangement to measure the torque generated by the rotor. The flow velocity was measured using a cup-type water velocity current metre.

6.2 Experimental procedure

The setup was installed in the elliptical canal, as shown in Fig. 29a and b. A trial was done with a negative overlap ratio of -0.17 , as the highest power coefficient was found for the -0.17 overlap ratio. As the rotor gets steady-state rotation, the readings were taken from no-load conditions to peak-load conditions. The readings were taken in a set of three trials each. By applying load, the time was noted for specific numbers of rotations for all readings. The trial was run until the rotor was stopped. The obtained results are discussed in the following subsection.

Fig. 29 View of test rig (laboratory scale artificial canal)



(a) Channel view of test rig

(b) Isometric view of test rig

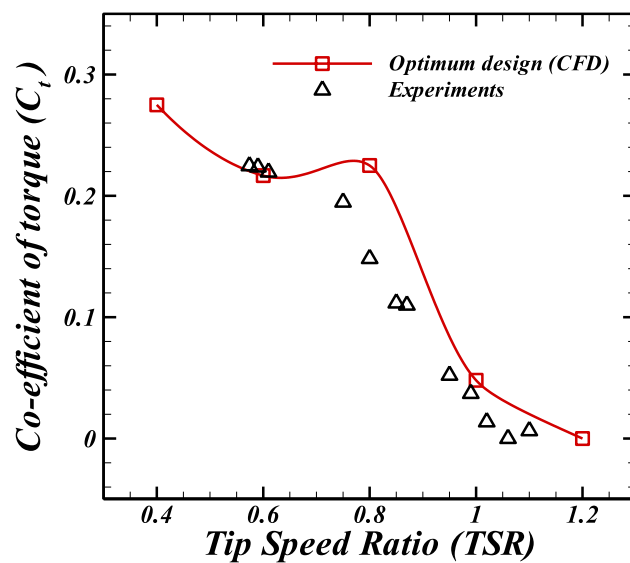


Fig. 30 Variation of torque coefficient with TSR

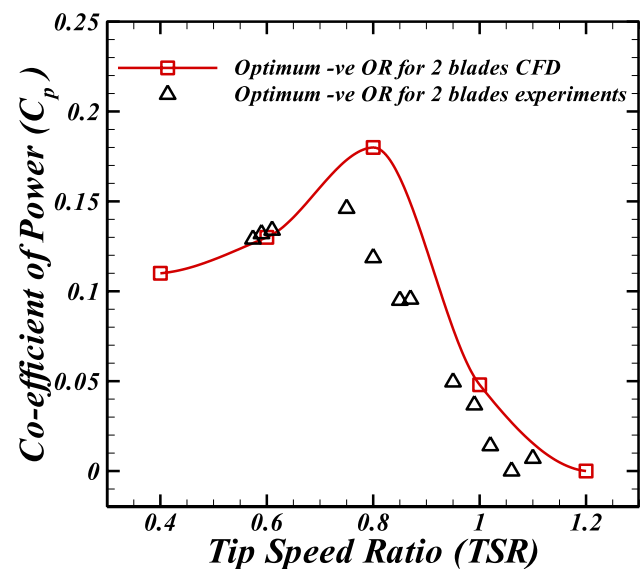


Fig. 31 Variation of power coefficient with TSR

6.3 Results and discussions

The primary task of experiments is to validate and check the results obtained by numerical simulations. The two performance parameters were compared with the experiments: torque coefficient and power coefficient.

The obtained graph for the same is shown in Figs. 30 and 31. Figure 30 shows a good match with the numerically obtained results. Although some uncertainties are always present in both numerical and experimental analysis, the power coefficient graph also shows a very similar trend, but the power coefficient's peak value was observed to be less than that of the numerical results. The presence of friction and experimental and numerical uncertainties are the major factors responsible for these variations.

7 Conclusion

In the present investigation, the performance of the Savonius turbine was investigated considering the negative overlap ratio. The hydrodynamic performance of the Savonius turbine investigated the negative overlap ratios with two vanned, three vanned, and four vanned turbines. The flow behaviour of water was analysed by plotting pressure and velocity contours around the rotor. The validating experiment was also conducted for obtained best design. With the present investigation, following conclusions can be derived:

Using the validated numerical methodology, the maximum value of the co-efficiency of power is 0.18 for two-bladed, 0.169 for three-bladed, and 0.15 for four-bladed rotors, which can be obtained at a tip speed value of 0.6 to 0.8 for all selected cases.

Moreover, the maximum power coefficient value is achieved with the gap between the blades at -60 mm or an overlap ratio of -0.17 for two-bladed rotors, with a -40 mm gap or -0.12 overlap ratio for three-bladed rotors, and -80 mm gap or -0.20 overlap for four-bladed rotors.

With the simulation of a three-bladed and four-bladed turbine, it is observed that the value of the coefficient of power at different vane overlaps is lower than that of the two-bladed rotor analysis.

The steep rise and fall of the performance are observed with the two-bladed turbine, near the heist performance range. It falls drastically with even a minor change in load or tip speed ratio. It indicates that the two-bladed turbine is suitable where the load on the turbine remains constant. The benefit of heist performance can be obtained by operating the turbine at a constant speed nearer to the best obtained tip speed ratio.

On the other hand, the maximum power coefficient obtained with three-bladed turbines is less than that obtained with two vane turbines. However, it provides nearly consistently good performance for a wide range of loads, i.e., tip speed ratio. A similar trend is also observed for the four-bladed turbine rotor. Hence, despite its maximum power coefficient being less than the two-vaned turbine rotors, the three-bladed turbine rotor is a comparatively better option where load fluctuation on the turbine is relatively high.

For single-speed energy-storing devices like a generator and a battery, the two-bladed Savonius with the best design performs better compared to the three- and four-bladed rotors. Hence, a two-bladed Savonius rotor was experimentally cross-verified and obtained a close match with numerical analysis, which validates the best obtained Overlap Ratio.

Acknowledgements Authors gratefully acknowledge Science and Engineering Research Board (SERB), Department of Science and Technology, Delhi, India for funding through core research grant specially to provide funding for computational and experimental resources.

Data availability All data, models, and code generated or used during the study appear in the submitted article.

References

- Alexander AS, Santhanakrishnan A (2018) Trapped cylindrical flow with multiple inlets for savonius vertical axis wind turbines. *J Fluids Eng*. <https://doi.org/10.1115/1.4038166>
- Alom N, Borah B, Saha UK (2018) An insight into the drag and lift characteristics of modified Bach and Benesh profiles of Savonius rotor. *Energy Procedia* 144:50–56. <https://doi.org/10.1016/j.egypro.2018.06.007>
- Álvarez-Álvarez E, Rico-Secades M, Fernández-Jiménez A, Espina-Valdes R, Corominas EL, Calleja-Rodríguez AJ (2020) Hydrodynamic water tunnel for characterization of hydrokinetic microturbines designs. *Clean Technol Environ Policy* 22:1843–1854. <https://doi.org/10.1007/s10098-020-01924-w>
- Bouzaher MT (2022) Effect of flexible blades on the Savonius wind turbine performance. *J Braz Soc Mech Sci Eng* 44(2):60
- Daskiran C, Riglin J, Oztekin A (2017) IMECE2015–51000. In: Proceedings of the ASME 2015 international mechanical engineering congress and exposition IMECE2015, pp 1–8
- Bouhal T, Rajad O, Kouksou T, Arid A, El Rhafiki T, Jamil A, Benbassou A (2018) CFD performance enhancement of a low cut-in speed current vertical tidal turbine through the nested hybridization of savonius and darrieus. *Energy Convers Manag* 169:266–278. <https://doi.org/10.1016/j.enconman.2018.05.027>
- Fatahian H, Hosseini E, Eshagh Nimvari M, Fatahian R, Fallah Jouybari N, Fatahian E (2022) Performance enhancement of Savonius wind turbine using a nanofiber-based deflector. *J Braz Soc Mech Sci Eng* 44(3):98
- Fukutomi J, Shigemitsu T, Daito H (2016) Study on performance and flow condition of a cross-flow wind turbine with a symmetrical casing. *J Fluids Eng Trans ASME* 133:1–9. <https://doi.org/10.1115/1.4004023>
- Gauthier E, Kinsey T, Dumas G (2017) Impact of blockage on the hydrodynamic performance of oscillating-foils hydrokinetic turbines. *J Fluids Eng Trans ASME* 138(9):091103. <https://doi.org/10.1115/1.4033298>
- Golecha K, Eldho TI, Prabhu SV (2012) Study on the interaction between two hydrokinetic savonius turbines. *Int J Rotating Mach*. <https://doi.org/10.1155/2012/581658>
- Gupta R, Biswas A, Sharma KK (2008) Comparative study of a three-bucket Savonius rotor with a combined three-bucket Savonius-three-bladed Darrieus rotor. *Renew Energy*. <https://doi.org/10.1016/j.renene.2007.12.008>
- Kamoji MA, Kedare SB, Prabhu SV (2009) Performance tests on helical Savonius rotors. *Renew Energy*. <https://doi.org/10.1016/j.renene.2008.06.002>
- Kinsey T, Dumas G (2016) Computational fluid dynamics analysis of a hydrokinetic turbine based on oscillating hydrofoils. *J Fluids Eng Trans ASME* 134:1–16. <https://doi.org/10.1115/1.4005841>
- Kumar A, Saini RP (2017) Performance analysis of a single stage modified Savonius hydrokinetic turbine having twisted blades. *Renew Energy* 113:461–478. <https://doi.org/10.1016/j.renene.2017.06.020>
- Layeghmand K, Ghiasi Tabari N, Zarkesh M (2020) Improving efficiency of Savonius wind turbine by means of an airfoil-shaped deflector. *J Braz Soc Mech Sci Eng* 42(10):528
- Liang X, Fu S, Ou B, Wu C, Chao CY, Pi K (2017) A computational study of the effects of the radius ratio and attachment angle on the performance of a darrieus-savonius combined wind turbine. *Renew Energy* 113:329–334. <https://doi.org/10.1016/j.renene.2017.04.071>
- Maître T, Amet E, Pellone C (2013) Modeling of the flow in a Darrieus water turbine: wall grid refinement analysis and comparison with experiments. *Renew Energy* 51:497–512. <https://doi.org/10.1016/j.renene.2012.09.030>
- Miller VB, Schaefer LA (2010) Dynamic modeling of hydrokinetic energy extraction. *J Fluids Eng Trans ASME* 132(9):1–7. <https://doi.org/10.1115/1.4002431>
- Naccache G, Paraschivoiu M (2017) Development of the dual vertical axis wind turbine using computational fluid dynamics. *J Fluids Eng Trans ASME* 139(12):121105. <https://doi.org/10.1115/1.4037490>
- Niebuhr CM, Van Dijk M, Neary VS, Bhagwan JN (2019) A review of hydrokinetic turbines and enhancement techniques for

- canal installations: technology, applicability and potential. *Renew Sustain Energy Rev* 113:109240
21. Patel V, Eldho TI, Prabhu SV (2019) Velocity and performance correction methodology for hydrokinetic turbines experimented with different geometry of the channel. *Renew Energy* 131:1300–1317. <https://doi.org/10.1016/j.renene.2018.08.027>
 22. Patel V, Bhat G, Eldho TI, Prabhu SV (2016) Influence of overlap ratio and aspect ratio on the performance of savonius hydrokinetic turbine. *Int J Energy Res* 41(6):829–844
 23. Patel V, Eldho TI, Prabhu SV (2017) Experimental investigations on darrieus straight blade turbine for tidal current application and parametric optimization for hydro farm arrangement. *Int J Mar Energy* 17:110–135
 24. Patel V, Eldho TI, Prabhu SV (2018) Performance enhancement of a Darrieus hydrokinetic turbine with the blocking of a specific flow region for optimum use of hydropower. *Renew Energy*. <https://doi.org/10.1016/j.renene.2018.12.074>
 25. Patel V, Eldho TI, Prabhu SV (2018) Theoretical study on the prediction of the hydrodynamic performance of a Savonius turbine based on stagnation pressure and impulse momentum principle. *Energy Convers Manag* 168:545–563
 26. Patel V, Savalia D, Panchal M, Rathod N (2016) Experimental investigations of hydrokinetic axial flow turbine. *Lecture notes in engineering and computer science*
 27. Rengma TS, Sengupta AR, Basumatary M, Biswas A, Bhanja D (2021) Performance analysis of a two bladed Savonius water turbine cluster for perennial river-stream application at low water speeds. *J Braz Soc Mech Sci Eng* 43:1–21
 28. Roy S, Saha UK (2015) Wind tunnel experiments of a newly developed two-bladed savonius-style wind turbine. *Appl Energy* 137:117–125. <https://doi.org/10.1016/j.apenergy.2014.10.022>
 29. Saini G, Saini RP (2018) A numerical analysis to study the effect of radius ratio and attachment angle on hybrid hydrokinetic turbine performance. *Energy Sustain Dev* 47:94–106. <https://doi.org/10.1016/j.esd.2018.09.005>
 30. Santhakumar S, Palanivel I, Venkatasubramanian K (2018) An experimental study on the rotational behaviour of a Savonius wind turbine for two-lane highway applications. *J Braz Soc Mech Sci Eng* 40:1–12
 31. Sarma NK, Biswas A, Misra RD (2014) Experimental and computational evaluation of Savonius hydrokinetic turbine for low velocity condition with comparison to Savonius wind turbine at the same input power. *Energy Convers Manag* 83:88–98. <https://doi.org/10.1016/j.enconman.2014.03.070>
 32. Sharma S, Sharma RK (2016) Performance improvement of Savonius rotor using multiple quarter blades—A CFD investigation. *Energy Convers Manag* 127:43–54. <https://doi.org/10.1016/j.enconman.2016.08.087>
 33. Shukla A, Alom N, Saha UK (2022) Spline-bladed Savonius wind rotor with porous deflector: a computational investigation. *J Braz Soc Mech Sci Eng* 44(10):444
 34. Talukdar PK, Sardar A, Kulkarni V, Saha UK (2018) Parametric analysis of model savonius hydrokinetic turbines through experimental and computational investigations. *Energy Convers Manag* 158:36–49. <https://doi.org/10.1016/j.enconman.2017.12.011>

Publisher's Note Springer Nature remains neutral with regard to jurisdictional claims in published maps and institutional affiliations.

Springer Nature or its licensor (e.g. a society or other partner) holds exclusive rights to this article under a publishing agreement with the author(s) or other rightsholder(s); author self-archiving of the accepted manuscript version of this article is solely governed by the terms of such publishing agreement and applicable law.